Supplementary Information

First-principles Screening of Novel Ferroelectric MXene Phases with Large Piezoelectric Response and Unusual Auxeticity

Lei Zhang [ab], *Cheng Tang* [ab], *Chunmei Zhang* [c], *Aijun Du* [*ab]

[a] School of Chemistry and Physics, Queensland University of Technology, Gardens Point Campus, Brisbane, QLD 4000, Australia

[b] Centre for Materials Science, Queensland University of Technology, Gardens Point Campus, Brisbane, QLD 4000, Australia

[c] Shanxi Key Laboratory for Theoretical Physics Frontiers, Institute of Modern Physics, Northwest University, Xi'an 710069, P. R. China

Corresponding Author: Aijun Du, email: aijun.du@qut.edu.au

Table S1. The total energy of fully optimized 2×2×1 supercells of $Hf_2CO_2H_2$, $Zr_2CO_2H_2$, Nb_2CS_2, Ta_2CS_2, Sc_2CO_2, Y_2CO_2, Sc_2CS_2, Y_2CS_2, and Mo_2NCl_2 with M-top, X-top, and mixed structures in different magnetic configurations (in eV). The energetically favorable magnetic configuration is highlighted in green color.

Composition	Configuration	Neel-AFM	zig-zag AFM	FM	NM
$Hf_2CO_2H_2$	M-top	-226.17	-226.67	-226.67	-226.67
	X-top	-226.17	-226.17	-226.17	-226.17
	Mixed	-226.72	-226.72	-226.72	-226.72
$Zr_2CO_2H_2$	M-top	-215.17	-215.17	-215.17	-215.17
	X-top	-214.71	-214.71	-214.71	-214.71
	Mixed	-215.24	-215.24	-215.24	-215.24
Nb_2CS_2	M-top	-174.29	-174.29	-174.29	-174.29
	X-top	-173.84	-173.84	-173.84	-173.84
	Mixed	-174.66	-174.66	-174.66	-174.66
Ta_2CS_2	M-top	-187.67	-187.67	-187.67	-187.67
	X-top	-187.06	-187.06	-187.06	-187.06
	Mixed	-188.02	-188.02	-188.02	-188.02
Sc_2CO_2	M-top	-163.92	-163.85	-163.92	-163.85
	X-top	-165.82	-165.82	-165.82	-165.82
	Mixed	-166.33	-166.33	-166.33	-166.33
Y_2CO_2	M-top	-164.92	-164.48	-165.02	-164.47
	X-top	-166.15	-166.15	-166.15	-166.15
	Mixed	-163.46	-163.78	-163.78	-166.72
Sc_2CS_2	M-top	-137.24	-137.24	-137.24	-137.24
	X-top	-140.76	-140.76	-140.76	-140.76
	Mixed	-142.16	-142.16	-142.16	-142.16
Y_2CS_2	M-top	-139.24	-139.10	-139.22	-139.10
	X-top	-142.45	-142.45	-142.45	-142.45
	Mixed	-143.99	-143.99	-143.99	-143.99
Mo_2NCl_2	M-top	-147.96	-147.96	-147.96	-147.96
	X-top	-145.16	-145.16	-145.16	-145.16
	Mixed	-148.94	-148.88	-148.88	-148.88

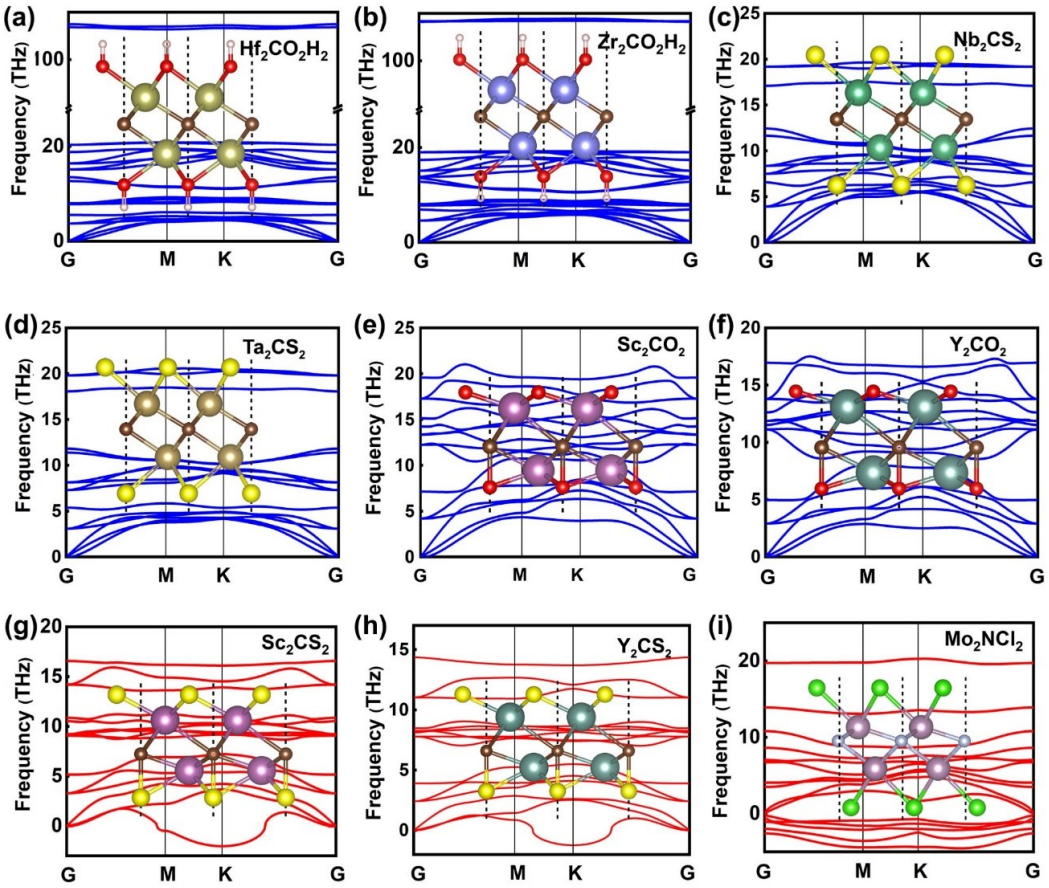

Figure S1. Phonon spectra of the surface-functionalized MXenes with energetically preferable mixed configuration. Insets are the optimized structures obtained from the high-throughput search.

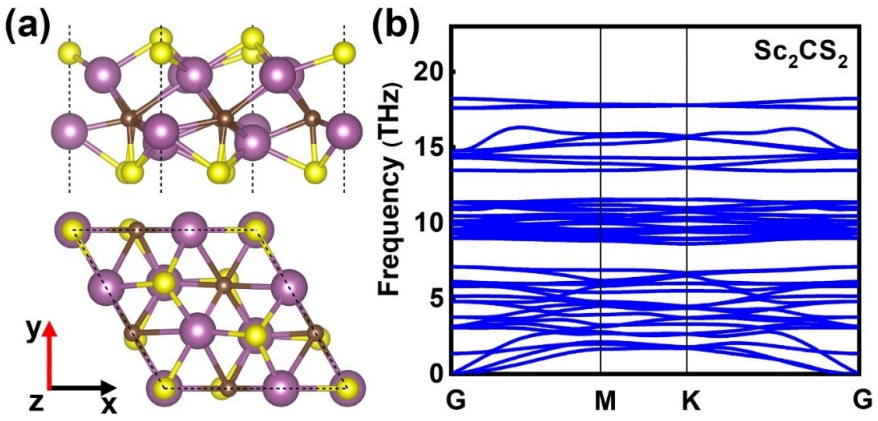

Figure S2. (a) and (b) Optimized structure of type-Ⅲ Sc_2CS_2 and its phonon spectrum respectively.

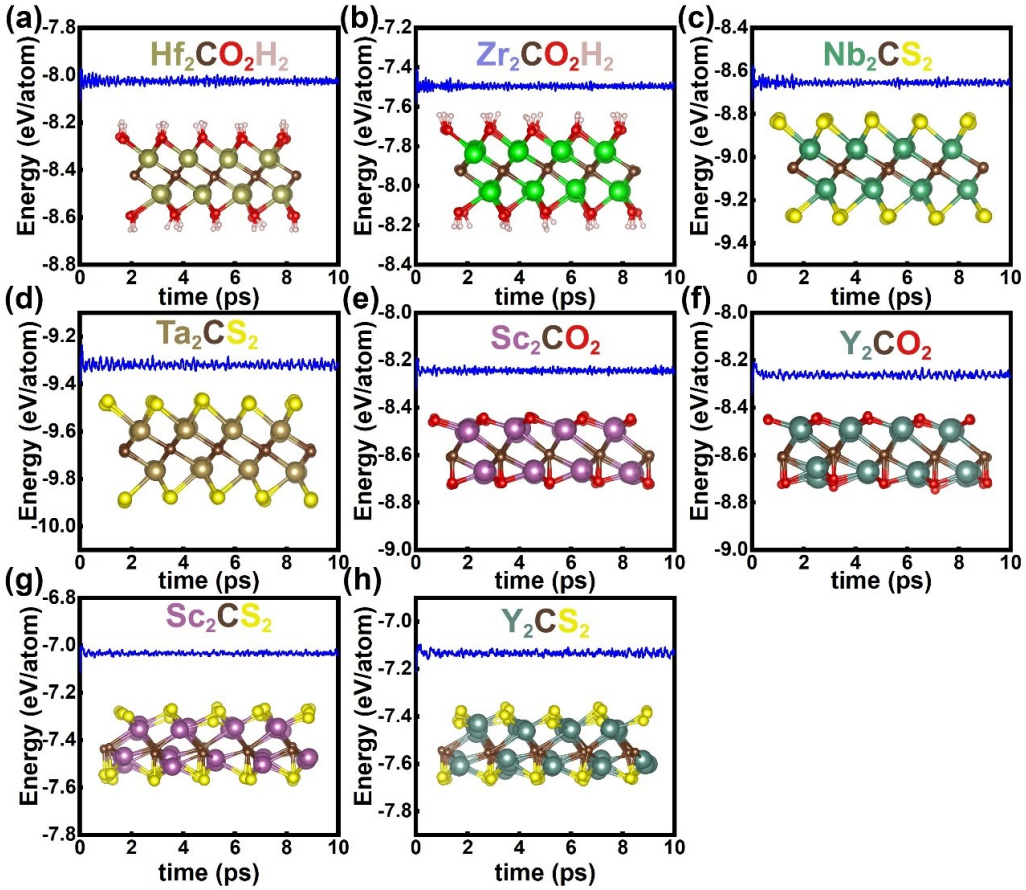

Figure S3. The evolution of the total energy per atoms of the AIMD at 600 K for all dynamically stable asymmetric MXenes (type-Ⅰ: Nb_2CS_2, Ta_2CS_2, $Zr_2CO_2H_2$, and $Hf_2CO_2H_2$; type-Ⅱ: Sc_2CO_2 and Y_2CO_2; type-Ⅲ: Sc_2CS_2 and Y_2CS_2)

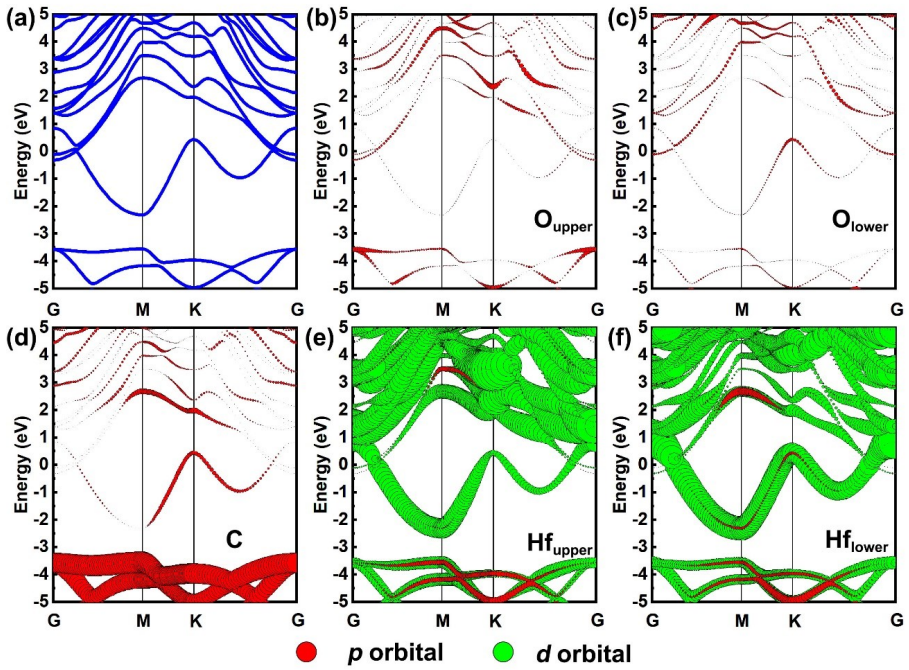

Figure S4. Band structure (a) and atomic decomposed band structures (b)-(f) of $Hf_2CO_2H_2$ calculated by HSE06 functional. The H atoms only contribute to the deep *s* states thus is not shown in these figures. The Fermi level is set to 0.

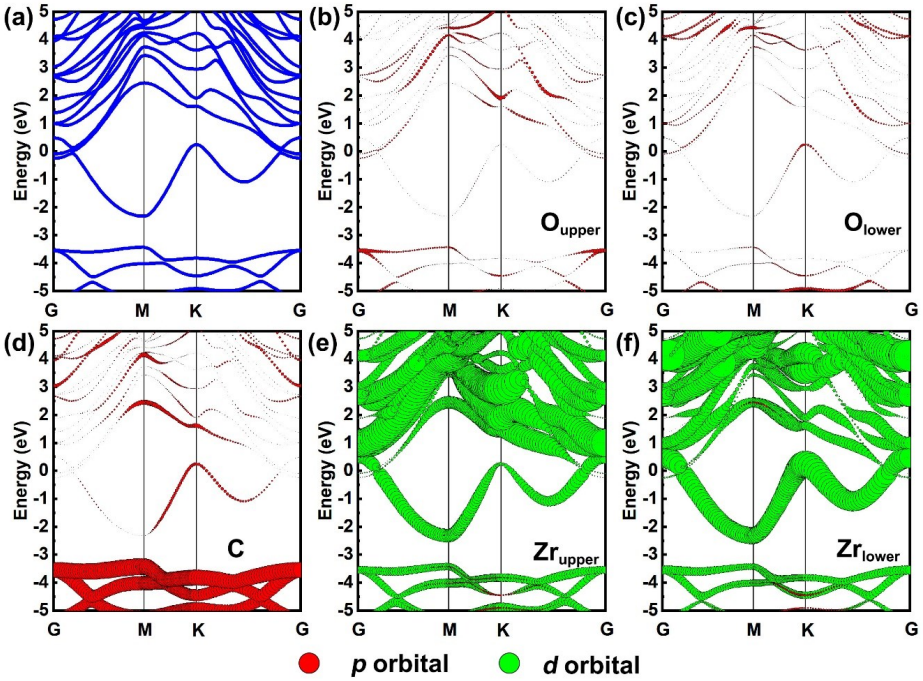

Figure S5. Band structure (a) and atomic decomposed band structures (b)-(f) of $Zr_2CO_2H_2$ calculated by HSE06 functional. The Fermi level is set to 0.

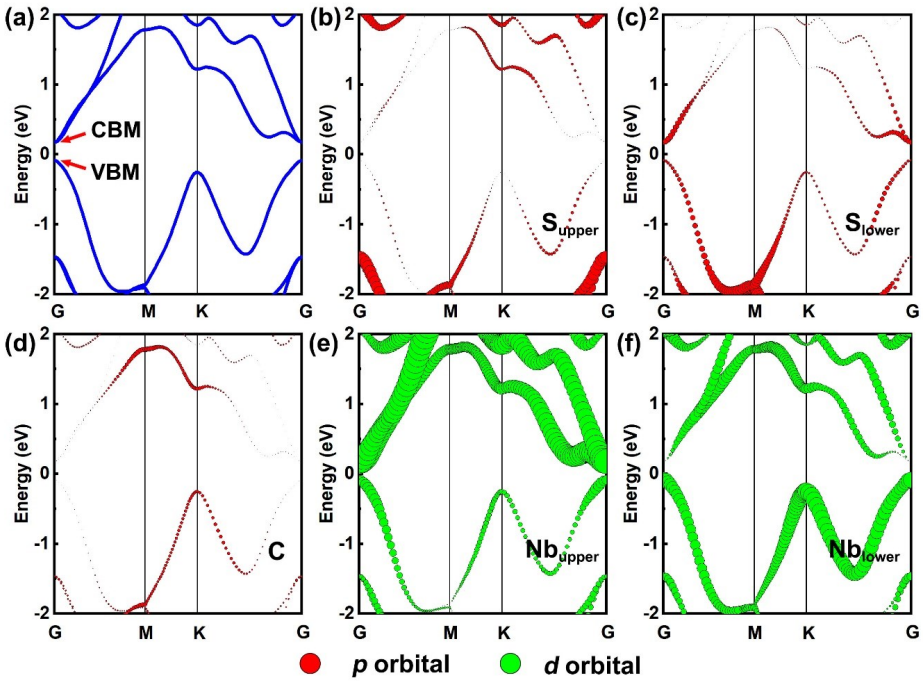

Figure S6. Band structure (a) and atomic decomposed band structures (b)-(f) of Nb_2CS_2 calculated by HSE06 functional. The Fermi level is set to 0.

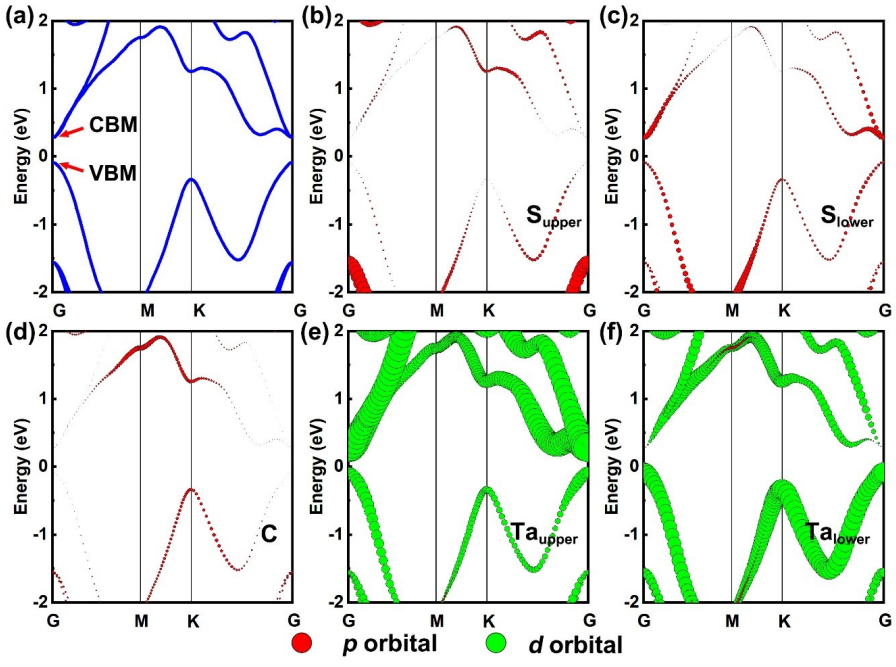

Figure S7. Band structure (a) and atomic decomposed band structures (b)-(f) of Ta_2CS_2 calculated by HSE06 functional. The Fermi level is set to 0.

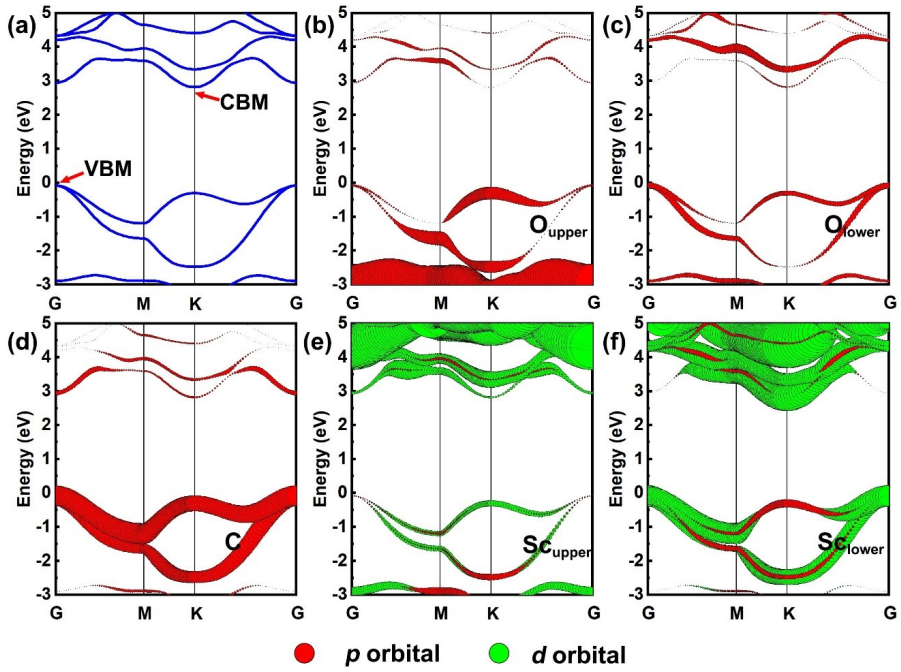

Figure S8. Band structure (a) and atomic decomposed band structures (b)-(f) of Sc_2CO_2 calculated by HSE06 functional. The Fermi level is set to 0.

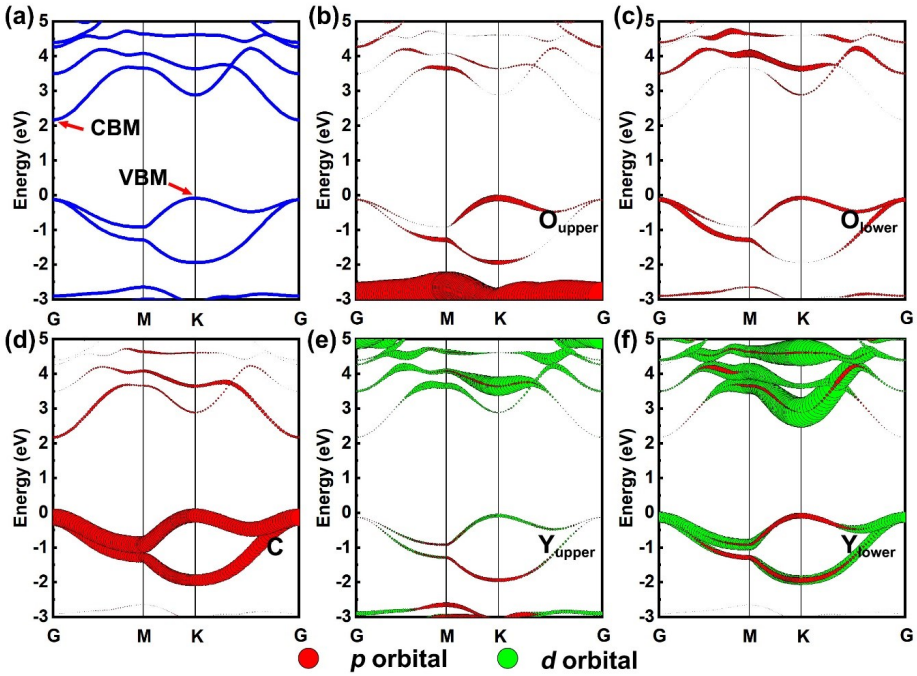

Figure S9. Band structure (a) and atomic decomposed band structures (b)-(f) of Y_2CO_2 calculated by HSE06 functional. The Fermi level is set to 0.

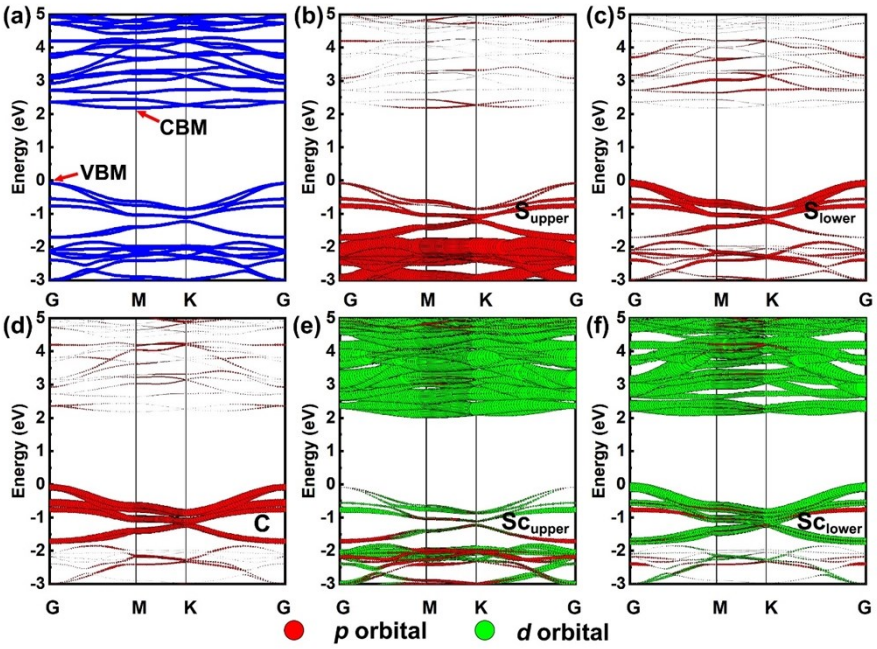

Figure S10. Band structure (a) and atomic decomposed band structures (b)-(f) of Sc_2CS_2 calculated by HSE06 functional. The Fermi level is set to 0.

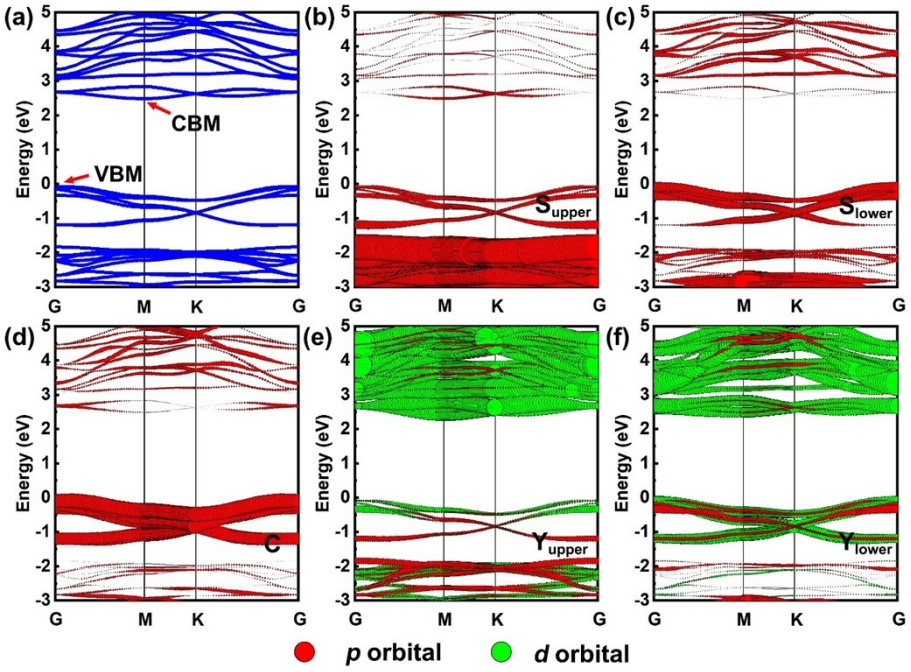

Figure S11. Band structure (a) and atomic decomposed band structures (b)-(f) of Y_2CS_2 calculated by HSE06 functional. The Fermi level is set to 0.

Note 1. As shown in Figure S4-11, the band edges of type-Ⅰ, Ⅱ, and Ⅲ MXenes show some discrepancies. The states near to the fermi level of type-Ⅰ MXenes are mostly contributed by the *d* orbitals of metal atoms. For type-Ⅲ MXenes, the conduction band minimum (CBM) comes from the *d* orbital of the upper and lower metal atoms, and the valence band maximum (VBM) is composed of the *p/d* states from the bottom part (carbon atoms, lower metal atoms and lower functional groups) of the structure. For type-Ⅱ MXene: Sc_2CO_2 and Y_2CO_2, the locations of their CBM and VBM are distinctive, leading to different band edge compositions. For Sc_2CO_2, the VBM is located at gamma point, contributed by the *p/d* states from the whole bottom part of the structure while the CBM is at K point and comes from the *d* orbital of the lower Sc atoms. For Y_2CO_2, its VBM is located at K point and contributed by the *p*/*d* orbitals of all the atoms in its structure, and the CBM at gamma point is composed of the *p* orbitals from the carbon atoms. We also checked the effect of SOC on the band structures of Nb_2CS_2 and Ta_2CS_2 and found SOC leads to band splitting as shown in Figure S12. However, their band gaps are only slightly changed (from 0.26 to 0.25 eV and from 0.37 to 0.35 eV for Nb_2CS_2 and Ta_2CS_2 respectively), indicating their robust semiconducting nature.

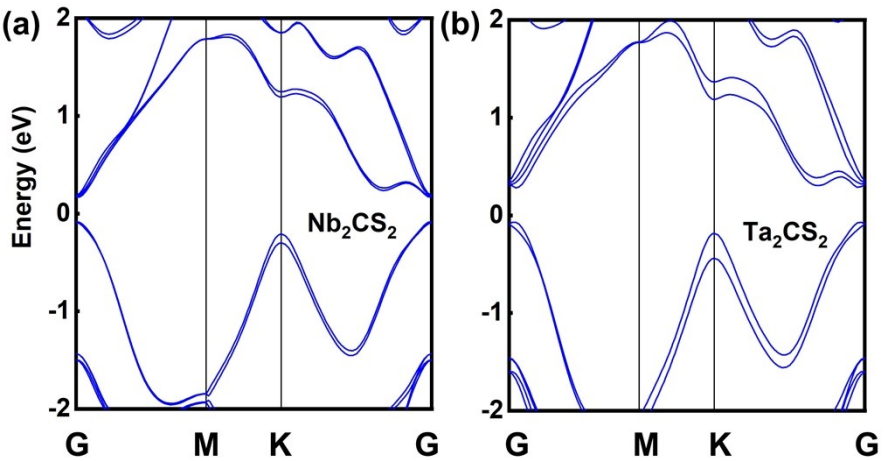

Figure S12. The band structures of Nb_2CS_2 and Ta_2CS_2 calculated with SOC effect.

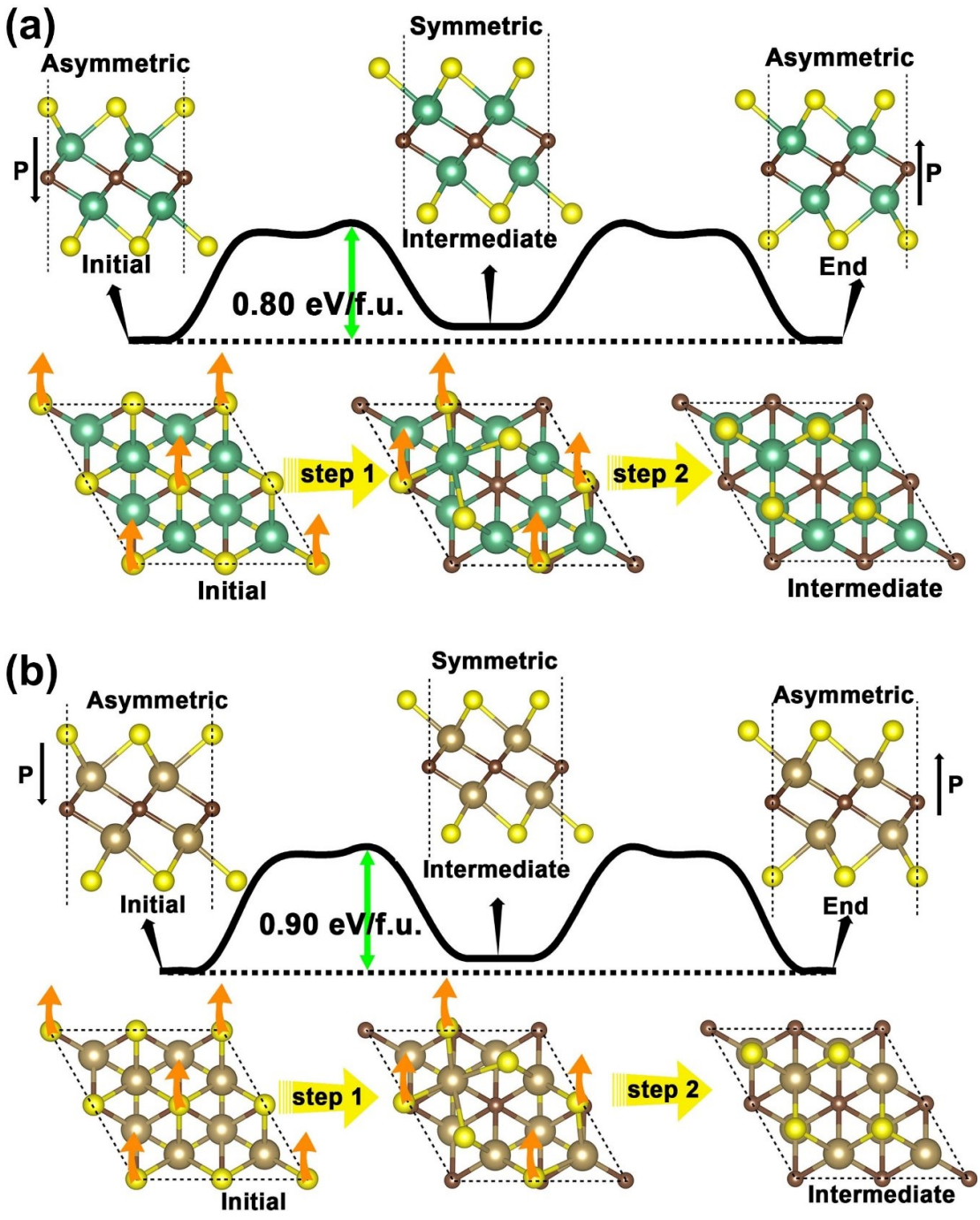

Figure S13. (a) and (b) NEB calculations of Nb_2CS_2 and Ta_2CS_2 respectively. In each figure, the upper panel: energy profiles of the polarization reversal from $-P_z$ ferroelectric state to the $+P_z$ ferroelectric state. The transformation proceeds through an intermediate M-top configuration with a symmetric structure. Bottom panel: Two-stage movements

of the upper surface sulfur atoms (indicated by orange arrows) from the -P_z ferroelectric state to the intermediate M-top state.

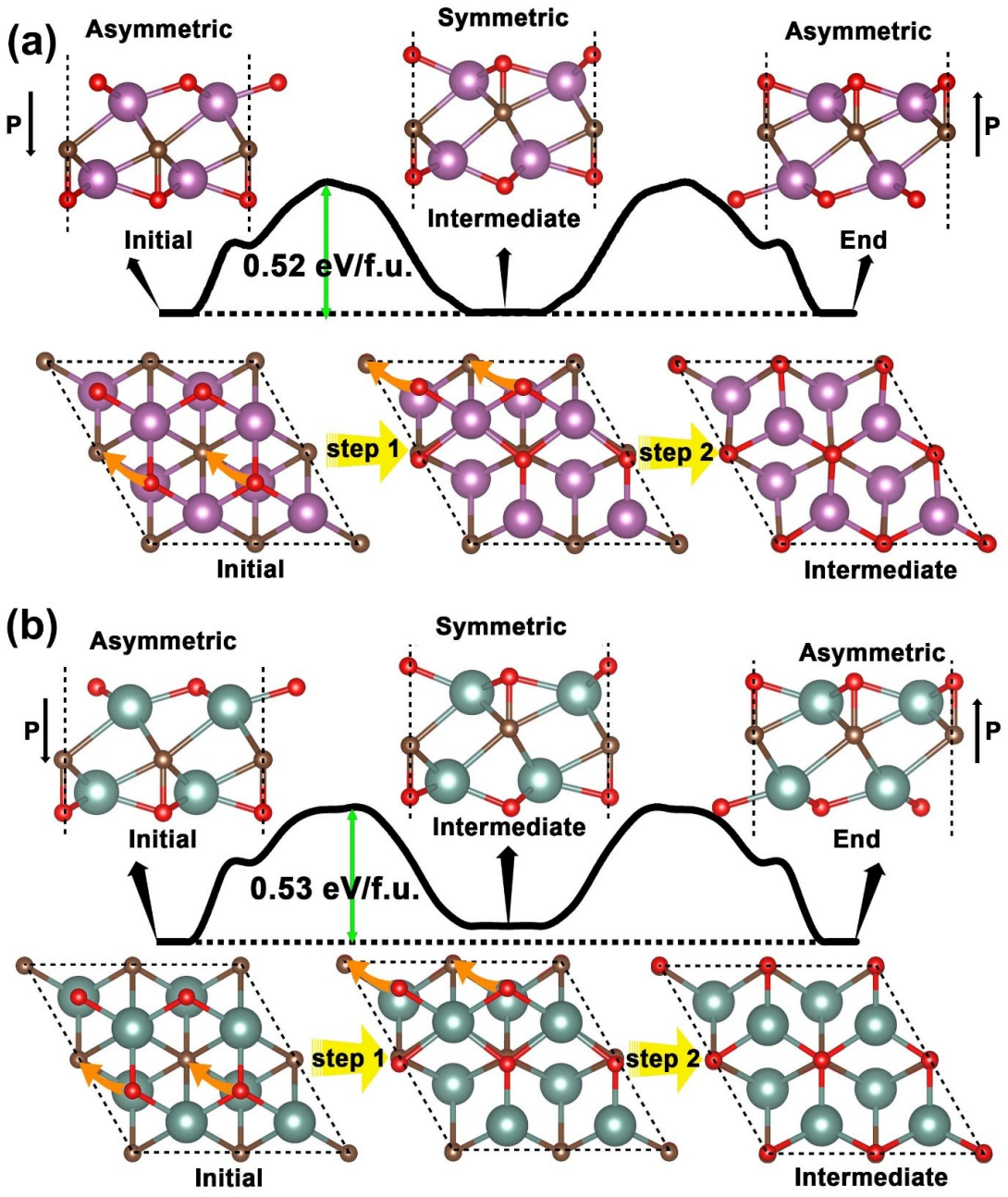

Figure S14. (a) and (b) NEB calculations of Sc_2CO_2 and Y_2CO_2 respectively. In each figure, the upper panel: energy profiles of the polarization reversal from -P_z ferroelectric state to the +P_z ferroelectric state. The transformation proceeds through a varied X-top configuration where the central carbon atoms are symmetrically bonded to the top and

bottom functional groups. Bottom panel: Two-stage movements of the upper surface oxygen atoms (indicated by orange arrows) from the -P_z ferroelectric state to the intermediate state.

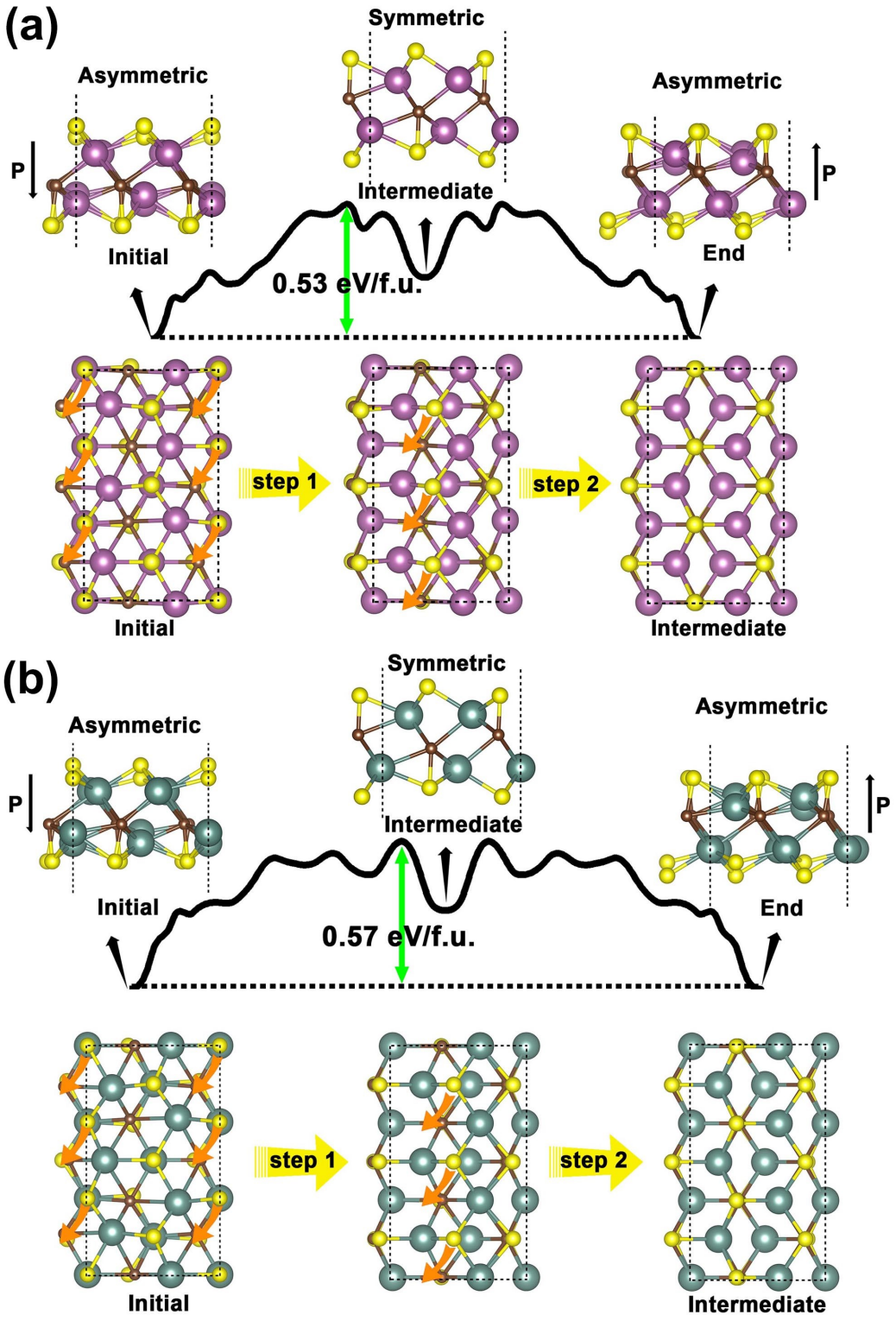

Figure S15. (a) and (b) NEB calculations of Sc_2CS_2 and Y_2CS_2 respectively. In each figure, the upper panel: energy profiles of the polarization reversal from $-P_z$ ferroelectric state to the $+P_z$ ferroelectric state. The transformation proceeds through a varied X-top configuration. Bottom panel: Two-stage movements of the upper surface sulfur atoms (indicated by orange arrows) from the $-P_z$ ferroelectric state to the intermediate state. The surface sulfur atoms do not move simultaneously thus leading to some fluctuation in the energy profile.

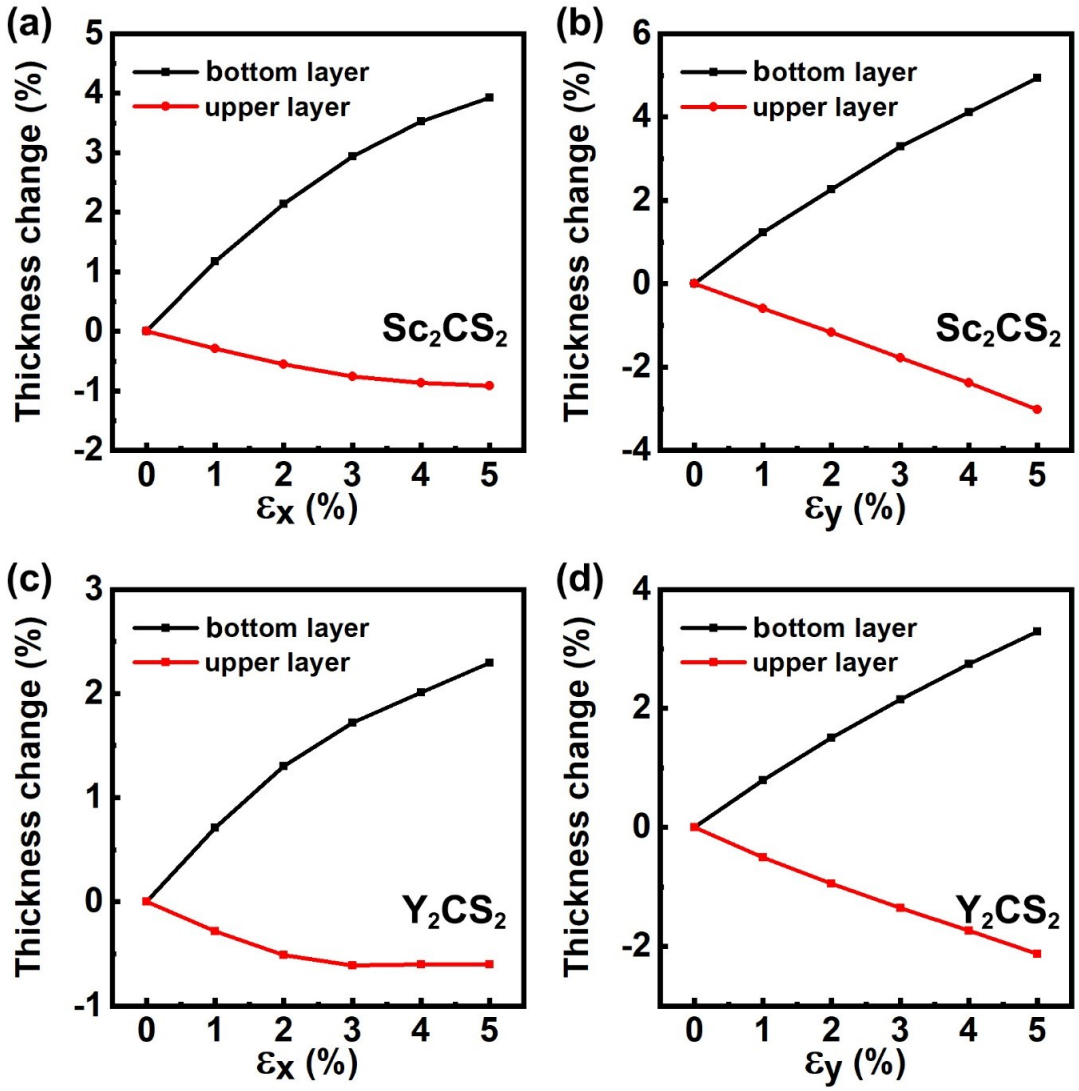

Figure S16. (a) and (b) The thickness change of the bottom and upper layers in Sc_2CS_2 as a function of in-plane strain ε_x and ε_y respectively. (c) and (d) The thickness change

of the bottom and upper layers in Y_2CS_2 as a function of in-plane strain ε_x and ε_y respectively.

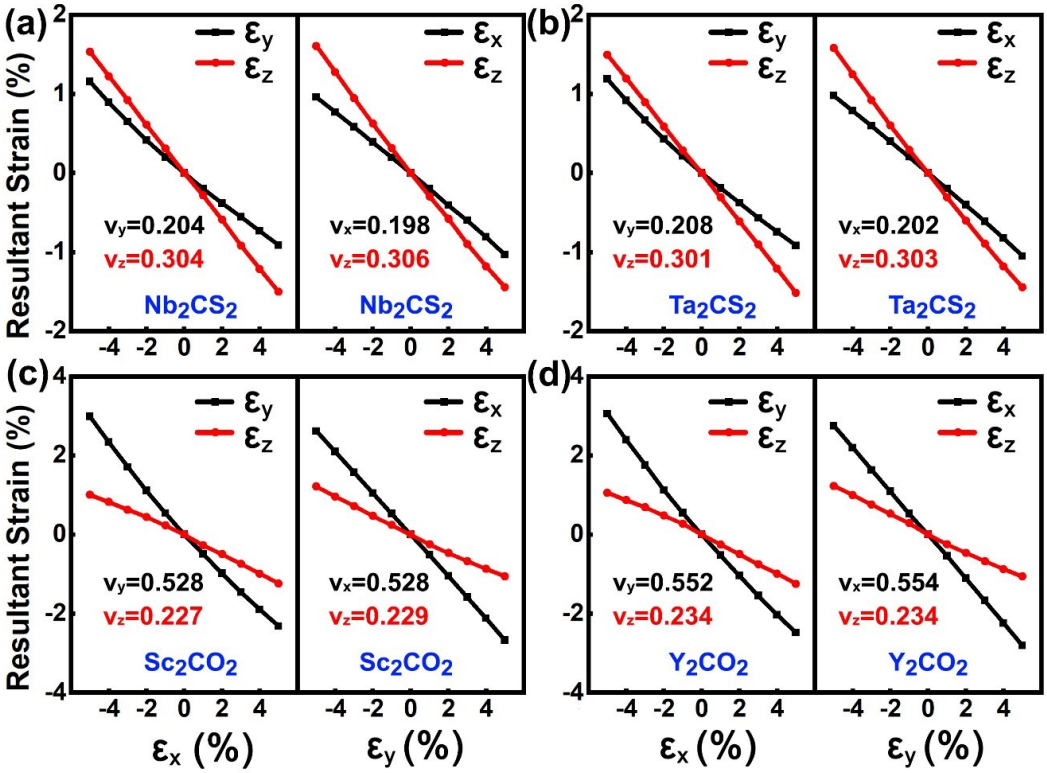

Figure S17. Resultant strain induced by a uniaxial strain along x (zig-zag) and y (arm-chair) directions in type-Ⅰ (Nb_2CS_2 and Ta_2CS_2) and type-Ⅱ (Sc_2CO_2 and Y_2CO_2) MXenes. Clearly, the type-Ⅰ and Ⅱ MXenes possess no NPR because their structures are not buckled.

Note 2. Although the Mixed configuration of $Hf_2CO_2H_2$ and $Zr_2CO_2H_2$ monolayers is the most stable configurations, the energy difference between the M-top and Mixed structures is relatively small (as shown in Table S1), which may raise challenge for the experimental fabrication of pure ferroelectric phase. However, considering the scarceness of polarized metal, it is still worthy to shed some theoretical light on the potential ferroelectricity in $Hf_2CO_2H_2$ and $Zr_2CO_2H_2$. The out-plane electric polarizations of $Hf_2CO_2H_2$ and $Zr_2CO_2H_2$ monolayers are calculated to be 0.93 and 0.32

pC/m which are smaller than that of Nb_2CS_2 and Ta_2CS_2. This can be attributed to the metallic nature of $Hf_2CO_2H_2$ and $Zr_2CO_2H_2$. The free electrons and holes may be attracted to the PCC and NCC which can diminish the strength of the electric dipole and result in a smaller P_{out} value. The polarization reversal is also studied by NEB methods. As shown in Figure S17 and S18, in the first step, the OH groups at the X-top side display a two-stage movement to achieve a symmetric M-top phase. Then the OH groups at the other side move to the X-top sites which is a complete reverse process of the first step. The switching barriers of $Hf_2CO_2H_2$ and $Zr_2CO_2H_2$ are 0.42 eV/f.u. and 0.40 eV/f.u. respectively. The barriers are smaller than other ferroelectric MXenes which may be caused by the weak interaction between the OH groups and the metal atoms.

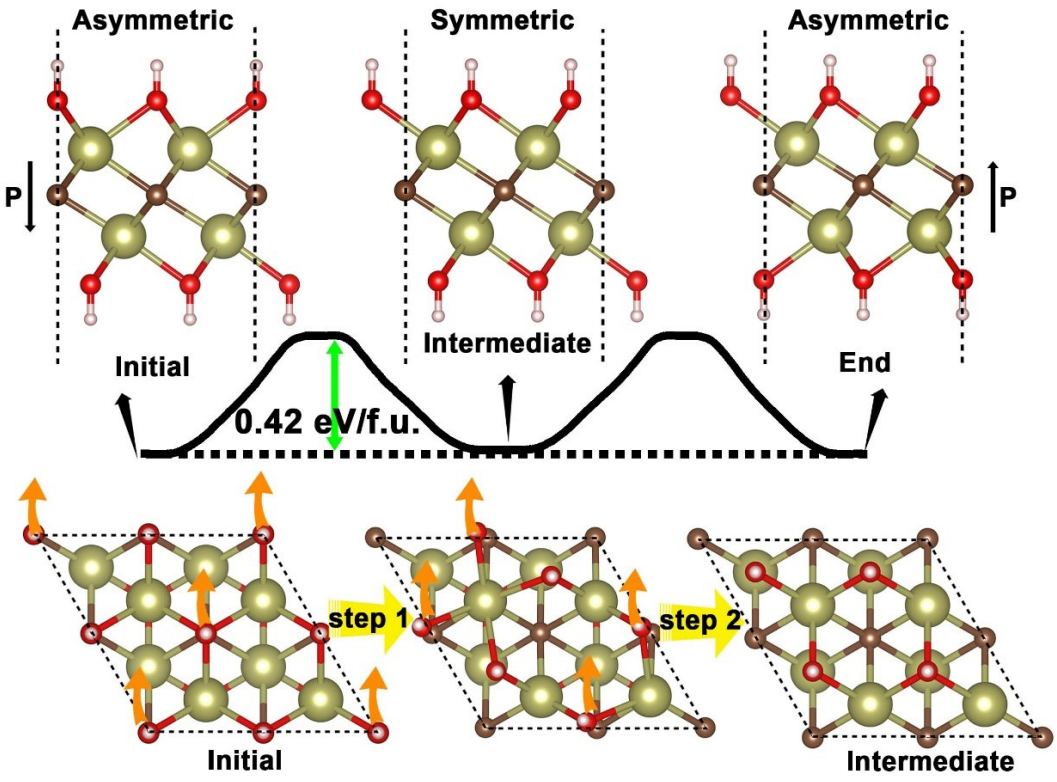

Figure S18. Upper panel: NEB calculation of $Hf_2CO_2H_2$ for the polarization reversal from $-P_z$ ferroelectric state to the $+P_z$ ferroelectric state. Bottom panel: Two-stage

movements of the upper surface OH groups (indicated by orange arrows) from the -P_z ferroelectric state to the intermediate M-top state.

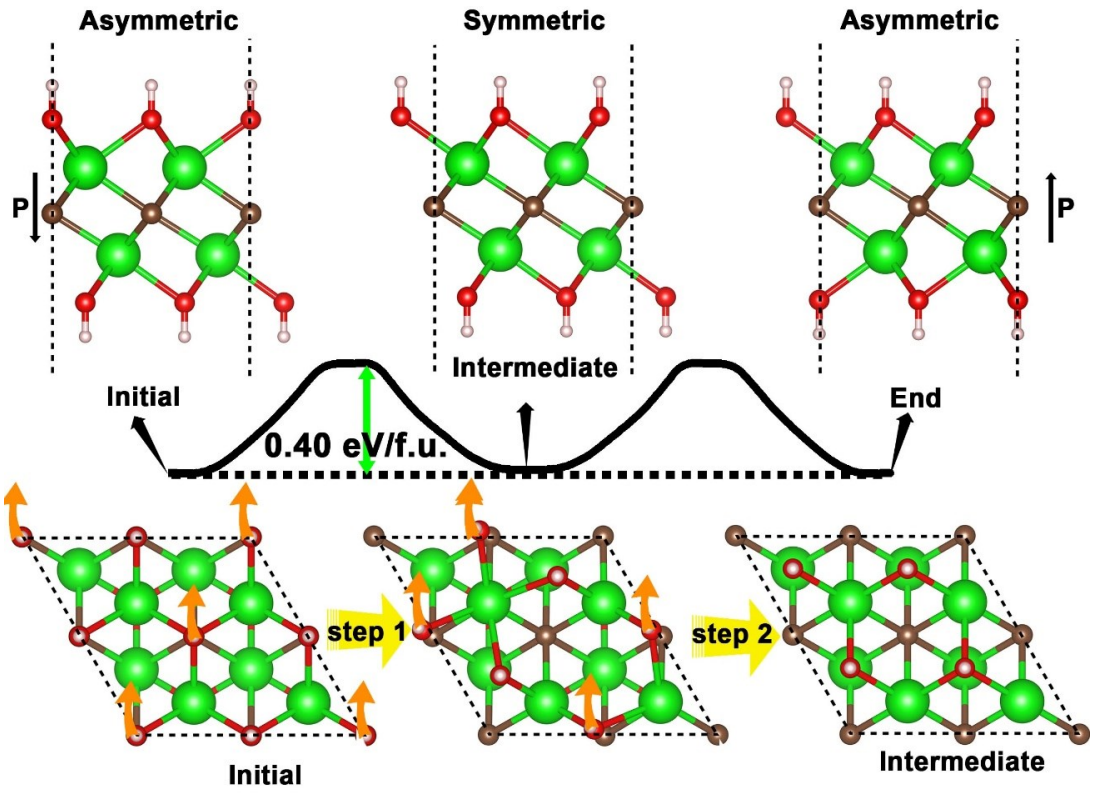

Figure S19. Upper panel: NEB calculation of $Zr_2CO_2H_2$ for the polarization reversal from -P_z ferroelectric state to the +P_z ferroelectric state. Bottom panel: Two-stage movements of the upper surface OH groups (indicated by orange arrows) from the -P_z ferroelectric state to the intermediate M-top state.